THE JOURNAL OF PHYSICAL CHEMISTRY C
A JOURNAL OF THE AMERICAN CHEMICAL SOCIETY

pubs.acs.org/JPCC Article

Efficient Electrochemical State of Health Model for Lithium Ion Batteries under Storage Conditions

Published as part of The Journal of Physical Chemistry virtual special issue "Esther Sans Takeuchi Festschrift".

Jin-Hyung Lim, Dongwook Koh, Suryanarayana Kolluri, Maitri Uppaluri, Akshay Subramaniam, and Venkat R. Subramanian*

Cite This: *J. Phys. Chem. C* 2023, 127, 2183−2193 Read Online

ACCESS | Metrics & More | Article Recommendations

ABSTRACT: Capacity degradation of batteries negatively impacts the lifetime of battery packs as well as the residual value of electric vehicles. Developing a degradation model for the prognosis of the state of health (SOH) under storage conditions is a critical aspect of developing algorithms to maximize the remaining useful lifetime of these systems. It is known that electrochemical degradation models have superior predictive ability compared to more empirical or data-driven models, but these still require improvement in terms of computational efficiency. In this work, we thus introduce a simple, reduced-order electrochemical degradation model for lithium-ion batteries. This model considers three key aging mechanisms with the ability to predict the SOH under various calendar aging conditions. Lumped model results are validated against a single particle-based degradation model and show close agreement, even as the simulation time is reduced by 2 orders of magnitude. This indicates significant potential in real-world applications to account and correct for the effects of storage on cell performance and lifetime.

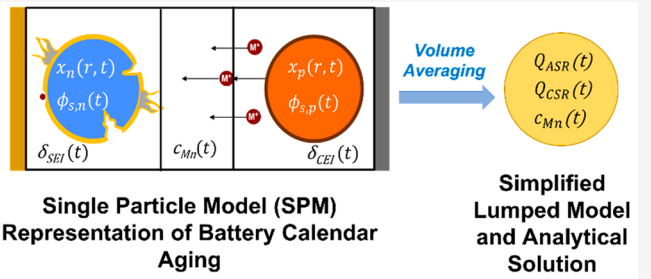

■ INTRODUCTION

In recent times, maximizing energy savings and emission reductions by maximizing battery utilization has served as a topic of concern for the electric vehicle (EV) industry. Additionally, with the increase in the production of power and energy from renewables, it becomes much more important to examine methods and techniques to store this energy. The Li-ion battery has played a key role in the field of electric transportation as well as energy storage solutions due to its higher power and energy density, safety, and reliability. Even though Li-ion batteries have shown superior reliability to other electrochemical systems, performance degradation cannot be avoided. The irreversible fade of the battery's performance will affect the residual value of the whole system. Accordingly, the state of health (SOH) of Li-ion batteries has been a critical topic for battery management systems.[1] SOH essentially denotes the ratio of current performance of a battery to the nominal value measured for a fresh cell. The capacity, power capability, and impedance of the cell all determine the SOH of the cell. In order to guarantee a prolonged system lifespan, it is necessary to develop battery management systems that can operate the battery while considering various aging processes.

For Li-ion batteries, the aging process can be divided into two modes, namely, calendric and cyclic aging. When an external current is applied, cells undergo a cyclic aging process which, in addition to modes such as SEI layer growth, induces the cracking of active material particles[2−4] as well as lithium plating at higher charging currents and low temperatures.[5] These mechanisms lead to severe degradation of the battery and deterioration in SOH and sometimes induce system failure and safety issues. Second, we have aging processes that are somewhat different from those observed during cycling. Though it is of reduced severity relative to cyclic aging, it still has importance in lifetime prediction because the cumulative duration of calendric aging conditions is much longer than the total time of operation. For example, in EV systems, a vehicle is parked most of the time, with only a small fraction of the usable life of the cell spent in driving and charging.

Several research works regarding SOH modeling have been reported and can broadly be divided into data-driven and first-principle approaches. First, many kinds of data-driven

Received: November 3, 2022
Revised: January 5, 2023
Published: January 25, 2023

Downloaded via UNIV OF TEXAS AT AUSTIN on January 25, 2025 at 17:54:34 (UTC).
See https://pubs.acs.org/sharingguidelines for options on how to legitimately share published articles.

ACS Publications © 2023 American Chemical Society

https://doi.org/10.1021/acs.jpcc.2c07752
J. Phys. Chem. C 2023, 127, 2183−2193

approaches have been reported, and they have utilized conventional regression techniques as well as machine learning algorithms. This approach has the advantage that the estimation and parametrization process is relatively simple and computationally efficient, but its prediction capability is relatively low. In addition, the training step for these models necessarily entails a significant amount of experimental data.[6] Second, first-principle approaches were proposed to model SOHs using various electrochemical models such as the pseudo-2D model, single particle model, and many other reduced models. Though it has relatively higher predictability, two main issues prevent wider usability. These are improving the computational efficiency of the model and model simplification to ensure proper parameter identification.

In this study, a new model reduction process is discussed, and its validity is demonstrated in terms of SOH prediction during calendric aging. A lumped OCV model is introduced and coupled with three key calendric aging mechanisms. The predictions from these models are then compared with the single particle-based aging model. Furthermore, a hybrid approach to integrate the lumped aging model into higher-level electrochemical models has also been discussed.

THEORY

Single Particle Model: Governing Equation and Constitutive Relations. In the single particle model (SPM), the positive and negative electrodes are assumed to be made up of uniform spherical particles with radius $R_{p,j}$,[7,8] where the subscript j ∈ (p, n) denotes the positive and negative electrodes. The diffusion of the lithium ions within the particles is described by Fick's second law in spherical coordinates with the boundary conditions given by eqs 1−3, where r is the radial dimension, t is the time dimension, and $c_{s,j}$ is the concentration of lithium ions in the electrode j. The parameter $D_{s,j}$ is the solid-phase diffusion coefficient

$$\frac{\partial c_{s,j}}{dt} = \frac{1}{r^2}\frac{\partial}{\partial r}\left(r^2 D_{s,j}\frac{\partial c_{s,j}}{dr}\right) \tag{1}$$

$$\left(D_{s,j}\frac{\partial c_{s,j}}{dr}\right)_{r=0} = 0 \tag{2}$$

$$\left(D_{s,j}\frac{\partial c_{s,j}}{dr}\right)_{r=R_j} = -j_{int,j} \tag{3}$$

$j_{int,j}$ is the pore wall flux of the lithium ions that is related to the average local current density. To solve this equation set, we set up a system of DAEs by discretizing the model and implementing it in time-adaptive solvers. For this work, we used the orthogonal collocation method for spatial discretization out of many options such as the finite differential approach, polynomial approximation,[9] and orthogonal collocation.[10] More details about the numerical aspects may be found in past work from our group.[11]

The state of charge for the positive and negative electrodes is defined as the Li-ion stoichiometry, i.e., the local lithium-ion concentration divided by the maximum lithium-ion concentration in the particle

$$x_j = \frac{c_{s,j}}{c_{s,j,max}} \tag{4}$$

The scaled surface concentration can thus be written as

$$x_{j,surf} = \frac{c_{s,j,surf}}{c_{s,j,max}} \tag{5}$$

Electrochemical Kinetics. When an electric current is passed through the load, electrochemical reactions occur at the particle/electrolyte interface, which leads to the intercalation or deintercalation of lithium ions. The reaction can be expressed as

$$\mathrm{Li}{-}\theta_s \rightleftharpoons \mathrm{Li}^+ + e^- + \theta_s \tag{6}$$

where Li−θ_s is a filled intercalation site and θ_s represents a vacant host on the solid particle surface. The rate of such a reaction is related to the surface SOC (state of charge, $x_{j,surf}$). This relation for pore−wall flux is expressed as

$$J_{int,j} = k_j c_{s,j,max} c_e^{\alpha_{a,j}}(1 - x_{j,surf})^{\alpha_{a,j}} x_{j,surf}^{\alpha_{c,j}}\left[\exp\left(\frac{\alpha_{a,j}F}{RT}\eta_j\right) - \exp\left(-\frac{\alpha_{c,j}F}{RT}\eta_j\right)\right] \tag{7}$$

$$\eta_j = \phi_{s,j} - \phi_{e,j} - U_j \tag{8}$$

The pore−wall intercalation flux is given by the Butler−Volmer equation (eq 7) expressed in terms of the overpotential η_j, where $\phi_{s,j}$ is the solid-phase potential, $\phi_{e,j}$ is the liquid (electrolyte) phase potential, and U_j is the open circuit potential (OCP) which is a function of surface SOC. In the isothermal SPM representation of the Li-ion battery, the electrolyte phase is ignored, and hence the electrolyte potential is set to $\phi_{e,j} = 0$.

For isothermal models, the cell potential equals the difference between the solid phase potentials of the positive and negative electrodes,

$$V_{cell} = \phi_{s,p} - \phi_{s,n} \tag{9}$$

Relevant cell design, kinetic, thermodynamic, and transport parameters for these models are summarized in Table 1 and Table 2. It must be noted that the SPM discussed thus far does not incorporate any models or terms for side reactions and capacity degradation. This framework will now be augmented with the aging mechanism discussed in subsequent sections, and this serves as the benchmark for evaluating the simplified models discussed in this work.

Side Reaction Equations. Li-ion battery aging has been widely studied to understand the underlying mechanisms and improve material characteristics, cell design, and battery management. Aging can be explained as the result of multiple mechanisms, such as side reactions between the active material and electrolyte, mechanical fracture of active material, and thermodynamic deposition of electrolyte. In this work, three main interfacial side reactions related to calendric aging are considered. The relevant models are now described in this section.

Cathode Side Reaction (CSR). In the cathode, the main reaction is the oxidation reaction of the electrolyte. The oxidized solvent at the surface of the cathode material supplies the excess charge to the cathode material.[12,13] As a result of this reaction, a Li^+ ion is intercalated into the cathode, which in turn decreases the equilibrium potential of the cathode[14] and leads to a gain of mobile Li capacity.[15,16] A list of electrolyte

https://doi.org/10.1021/acs.jpcc.2c07752
J. Phys. Chem. C 2023, 127, 2183−2193

Table 1. Relevant Parameters for the Model

Parameter			Anode	Separator	Cathode
Geometry					
electrode cross sectional area	A_c	m^2	2.0		
thickness	L	m	69×10^{-6}	17.4×10^{-6}	57
particle radius	R_p	m	10×10^{-6}		3.8×10^{-6}
solid volume fraction	ε_s		0.63		0.64
filler volume fraction	ε_f		0.07		0.06
specific surface area correction	S_i		13.15		28.80
Thermodynamics					
maximum solid concentration	$c_{s,max}$	mol/m^3	3.1×10^4		4.9×10^4
Kinetics					
activation rate constant	k	m/s	3.0×10^{-10}		1.3×10^{-10}
activation energy of rate constant	$E_{a,k}$	J/mol	1.0×10^4		9.0×10^4
anodic charge-transfer coefficient	α_a		0.5		0.5
cathodic charge transfer coefficient	α_c		0.5		0.5
Transport					
solid diffusivity	D_s	m^2/s	3.0×10^{-14}		2.0×10^{-13}
electrolyte concentration	c_e	mol/m^3	1000		
reference temperature	T_{ref}	K	25 + 273.15		
cathode equilibrium potential	$U_p(x_p)$	V	$-10.0x_p^4 + 22.2x_p^3 - 15.8x_p^2 + 2.77x_p + 4.33$		
anode equilibrium potential	$U_n(x_n)$	V	$0.436 + 20.1\exp(-51.6x_n) + 0.382\exp(-665x_n) - 1.39\exp(40.36x_n - 43.2) - 0.104\arctan(8790x_n - 586) - 0.146\arctan(3.67x_n + 0.0244)$		

oxidation reactions was proposed by Xu et al.[13] The representative formula of the solvent (SL) oxidation reaction can be expressed as

$$\mathrm{SL} \xrightarrow{\text{oxidation}} \mathrm{SL_o} + \mathrm{H^+(or\ SL^+)} + \mathrm{e^-} \tag{10}$$

According to Lin et al.,[17] cathode side reaction can be written as

$$J_{CSR} = J_{CEI,0}\exp\left[-\frac{E_{a,CEI}}{R}\left(\frac{1}{T} - \frac{1}{T_{ref}}\right)\right]\exp\left[+\frac{\alpha_{CEI}F}{RT}\eta_{CEI}\right]\exp[-\lambda_{CEI}\delta_{CEI}] \tag{11}$$

$$\eta_{CEI} = \phi_{s,n} - \phi_{e,n} - U_{CEI} \tag{12}$$

And the charge balance equation of the cathode is now modified as

$$J_{tot,p} = J_{int,p} + J_{CSR} = \frac{I_{app}}{S_p}\frac{1}{F} \tag{13}$$

Anode Side Reaction (ASR). Electrolyte reduction on the anode particle surface forms a passivation layer, known as the solid-electrolyte interphase (SEI). During this reaction, electrolyte solvent molecules and Li from the anode are consumed. In contrast to other parasitic reactions such as lithium plating and phenomena such as surface cracking, this mechanism is active regardless of the application of an external current, leading us to assume that SEI formation is the dominant degradation mechanism in calendar aging.

Table 2. Relevant Electrochemical Parameters for the Side Reaction Models

Parameter			Value
SEI Formation			
reaction rate constant for SEI formation	k_{SEI}	$mol/(s^1\ m^2)$	8.7×10^{-13}
multiplier applied to the SEI current associated with cathode Mn dissolution	χ_{CatMn}		1
activation energy for SEI formation	$E_{a,SEI}$	J/mol	8.2×10^4
charge transfer coefficient for SEI formation	α_{SEI}		0.25
limiting coefficient for SEI formation	γ_{SEI}	1/(Ah)	0.2
conductivity of SEI	K_{SEI}	S/m^2	1.75×10^{-4}
density of SEI	ρ_{SEI}	kg/m^3	1690
molar mass of SEI	M_{SEI}	kg/mol	0.162
Mn Dissolution			
reaction rate constant for Mn dissolution	k_{MnDsol}	$mol/(s^1\ m^2)$	4.0×10^{-8}
activation energy for Mn dissolution	$E_{a,Mn}$	J/mol	3.0×10^4
charge transfer coefficient for Mn dissolution	α_{MnDsol}		0.58
CEI Formation			
reaction rate constant for CEI formation	k_{CEI}	$mol/(s^1\ m^2)$	3.6×10^{-14}
activation energy for CEI formation	$E_{a,CEI}$	J/mol	9.5×10^4
charge transfer coefficient for CEI formation	α_{CEI}		0.42
limiting coefficient for CEI formation	λ_{CEI}	1/(Ah)	0.16
conductivity of CEI	K_{CEI}	S/m^2	1.75×10^{-4}
density of CEI	ρ_{CEI}	kg/m^3	1690
molar mass of CEI	M_{CEI}	kg/mol	0.162

It is known that the SEI is an ion conductor and allows the transport of Li ions from the bulk electrolyte to the anode surface. In addition, SEI increases the cell impedance and suppresses further production of additional SEI. These phenomena are explained by the transition of the SEI layer growth from being limited by the kinetics of the reduction reaction to diffusion limitations as well as a decrease in ionic conductivity in the SEI layer. Safari et al. and Prada et al. assumed that SEI formation can be determined by both kinetic and diffusion limitations.[18,19] SEI thickness growth decreases ion conductivity and solvent diffusion through the SEI, finally suppressing new SEI formation.

To describe these mechanisms, Prada et al. introduced an additional diffusion equation of the solvent in the SEI, and the concentration of solvent was considered in the side reaction equation. Lin et al. introduced the thickness limitation coefficient, which makes the side reaction current exponentially decrease with the thickness of the SEI.[17] Due to their exponential form, either equation can be adapted to reproduce a square-shaped aging trend reported previously.[20,21]

SEI formation can be accelerated by the deposition of Mn^{2+} ions dissolved from the positive electrode, and this was explained by the electrocatalytic effect of Mn.[22] Crawford et al. implemented a model for SEI growth enhancement by Ni^{2+} ions based on a multiplication factor that depends on the concentration of deposited Ni on the anode surface.[23] Thus,

https://doi.org/10.1021/acs.jpcc.2c07752
J. Phys. Chem. C 2023, 127, 2183−2193

the modified SEI constitutive equation for SEI growth can be written as

$$J_{SEI} = -J_{SEI,0}(1 + k_{Ni,SEI}n_{Ni})\exp\left(-\frac{\alpha_{SEI}F}{RT}\eta_{SEI}\right) \quad (14)$$

In initial experiments to quantify the extent of Mn^{2+} dissolution in our graphite/NMC Li-ion cells, we conducted a teardown of an aged battery (80% of initial capacity) and sampled the electrolyte and negative electrode. The dissolved Mn^{2+} concentration and the amount deposited on the negative electrode were measured from the sampled electrolytes and electrodes using ICP/MS techniques (data not shown in this work). The dissolved Mn^{2+} concentration was found not to exceed 2000 pm. Based on this result, we assume that the contribution to capacity loss of Mn^{2+} dissolution at the cathode and its deposition at the anode can be ignored. For the negative electrode, the only effect of the deposited Mn is thus in catalyzing SEI formation. Moreover, we assume that the deposited transition-metal concentration is proportional to the concentration of dissolved Mn^{2+}. Based on these considerations, we thus rewrite the SEI constitutive equation as

$$J_{SEI} = -J_{SEI,0}(1 + \chi_{cat,Mn}c_{MnDsol})\exp\left[-\frac{E_{a,SEI}}{R}\left(\frac{1}{T} - \frac{1}{T_{ref}}\right)\right] \exp\left[-\frac{\alpha_{SEI}F}{RT}\eta_{SEI}\right]\exp[-\lambda_{SEI}\delta_{SEI}] \quad (15)$$

with

$$\eta_{SEI} = \phi_{s,n} - \phi_{e,n} - U_{SEI} \quad (16)$$

where $c_{(MnDsol)}$ represents the concentration of dissolved Mn in the electrolyte. In principle this value can be calculated based on a mass balance for manganese ions using a constitutive equation such as Fick's law for ion fluxes,[17] but for calendar aging, this can easily be approximated by a simple overall balance using a lumped approach as

$$\frac{d}{dt}c_{MnDsol} = J_{MnDsol}\frac{a_{s,p}\epsilon_{s,p}L_p}{\epsilon_n L_n + \epsilon_s L_s + \epsilon_p L_p} \quad (17)$$

where J_{MnDsol} is the dissolution flux at the surface of the cathode and can be expressed as

$$J_{MnDsol} = J_{MnDsol,0}\exp\left[\frac{E_{a,MnDsol}}{R}\left(\frac{1}{T} - \frac{1}{T_{ref}}\right)\right]\exp\left[+\frac{\alpha_{MnDsol}F}{RT}\eta_{MnDsol}\right] \quad (18)$$

$$\eta_{MnDsol} = \phi_{s,p} - \phi_{e,p} - U_{MnDsol} \quad (19)$$

Analogous to eq 13, the anode charge balance is now modified as

$$J_{tot,n} = J_{int,n} + J_{SEI} = -\frac{I_{app}}{S_n}\frac{1}{F} \quad (20)$$

These models may easily be integrated into the SPM framework described in the previous section. Standard discretization and time integration methods can be used to simulate these models for a given initial or operating condition.

Lumped Approximation of the Degradation Model. *Equilibrium Potential Approximation Using the OCV Aging Model.* During calendar aging, the external applied current is zero. The anode potential and concentrations are thus spatially uniform. Considering the negligible intercalation flux under the storage conditions, we can reasonably assume that activation overpotential approaches zero

$$\eta = \phi_{s,i} - \phi_{e,i} - U_i = 0 \quad (21)$$

The cell potential can thus be expressed as

$$V_{cell} = U_p(\bar{x}_p) - U_n(\bar{x}_n) \quad (22)$$

The volume-averaged normalized solid concentrations x_p and x_n will change as the cell ages and need to be updated accordingly. These can be calculated using the open circuit voltage (OCV) aging model proposed by Rumberg et al.[16,24,25] OCV of the aged cell can be simulated after considering relevant side reactions. This model can then be implemented to determine the equilibrium potential of the cathode and anode at the given aged state and a fixed value of the nominal full cell SOC.

We begin with the general definition of cathode or anode OCV as a function of its stoichiometry, usually used in the various electrochemical models.

$$U_p = U_p(x_p),\ \ U_n = U_n(x_n) \quad (23)$$

To describe the detailed derivation process, the meaning of continuous charge balance (CCB) is first explained. During cycling, the continuous charge balance represents the time integral of the external current. For example, for a charging current of 1 A applied for 1 h, the CCB will show an increase of 1 Ah. Under calendric aging conditions, the contribution of an external current to the CCB is zero. Changes in CCB thus reflect the number of Li ions consumed or generated due to side reactions. For a fresh cell, the relationship between continuous charge balance and volume-averaged stoichiometry of the cathode or anode is given by

$$c_{s,max,p}L_pA_c\epsilon_{s,p}\frac{F}{3600}x_{p,BOL} + Q_{offset,p0} = Q_{CCB}(x_{p,BOL}) \quad (24)$$

$$c_{s,max,n}L_nA_c\epsilon_{s,n}\frac{F}{3600}x_{n,BOL} + Q_{offset,n0} = Q_{CCB}(x_{n,BOL}) \quad (25)$$

The charge equality condition needs to be satisfied, which for a given full cell SOC_{FC} is given by

$$Q_{CCB}(x_{p,SOC_{FC}}) = Q_{CCB}(x_{n,SOC_{FC}}),\ \ 0 < SOC_{FC} < 1 \quad (26)$$

where

$$x_{i,SOC_{FC}} = x_{i,SOC0} + SOC_{FC}(x_{i,SOC100} - x_{i,SOC0}) \quad (27)$$

We can also define the cell capacity based on the cyclable Li amount, and this equation is valid for any aging state.

$$Q_{fullcell} = c_{s,max,p}L_pA_c\epsilon_{s,p}\frac{F}{3600}(x_{p,SOC0} - x_{pSOC100}) = c_{s,max,n}L_nA_c\epsilon_{s,n}\frac{F}{3600}(x_{n,SOC100} - x_{n,SOC0})[Ah] \quad (28)$$

When the cathode offset in the fresh state is set to zero, ($Q_{offset,p0} = 0$), the initial offset of the anode is then given by

https://doi.org/10.1021/acs.jpcc.2c07752
J. Phys. Chem. C 2023, 127, 2183−2193

$$Q_{\text{offset,n0}} = c_{\text{s,max,p}} L_{\text{p}} A_{\text{c}} \epsilon_{\text{s,p}} \frac{F}{3600} x_{\text{p,SOC0,BOL}} - c_{\text{s,max,n}} L_{\text{n}} A_{\text{c}} \epsilon_{\text{s,p}} \frac{F}{3600} x_{\text{n,SOC0,BOL}} \tag{29}$$

If we assume that there was no cathode side reaction during the formation process, then $Q_{\text{offset,n0}}$ indicates the amount of Li consumed during the SEI formation.

In any aged state, we can rewrite the continuous charge balance as

$$Q_{\text{CCB}}(x_{\text{p}}) = c_{\text{s,max,p}} L_{\text{p}} A_{\text{c}} \epsilon_{\text{s,p}} \frac{F}{3600} x_{\text{p}} + Q_{\text{CSR}}(t) \tag{30}$$

$$Q_{\text{CCB}}(x_{\text{n}}) = c_{\text{s,max,n}} L_{\text{n}} A_{\text{c}} \epsilon_{\text{s,n}} \frac{F}{3600} x_{\text{n}} + Q_{\text{offset,n0}} + Q_{\text{ASR}}(t) \tag{31}$$

Thus, we have

$$U_{\text{full cell}}(Q_{\text{CCB}}) = U_{\text{p}}\left(\frac{3600}{F} \frac{1}{c_{\text{s,max,p}} L_{\text{p}} A_{\text{c}} \epsilon_{\text{s,p}}} (Q_{\text{CCB}} - Q_{\text{CSR}}(t))\right) - U_{\text{n}}\left(\frac{3600}{F} \frac{1}{c_{\text{s,max,n}} L_{\text{n}} A_{\text{c}} \epsilon_{\text{s,n}}} (Q_{\text{CCB}} - Q_{\text{offset,n0}} - Q_{\text{ASR}}(t))\right) \tag{32}$$

Furthermore, we can find the value of the updated $x_{\text{i,SOC0}} x_{\text{i,SOC100}}$ given by

$$U_{\text{FC,SOC100}} = U_{\text{p}}(x_{\text{p,SOC100}})|_{t=0} - U_{\text{n}}(x_{\text{n,SOC100}})|_{t=0} = U_{\text{p}}(x'_{\text{p,SOC100}})|_{t=t'} - U_{\text{n}}(x'_{\text{n,SOC100}})|_{t=t'} \tag{33}$$

$$U_{\text{FC,SOC0}} = U_{\text{p}}(x_{\text{p,SOC0}})|_{t=0} - U_{\text{n}}(x_{\text{n,SOC0}})|_{t=0} = U_{\text{p}}(x'_{\text{p,SOC0}})|_{t=t'} - U_{\text{n}}(x'_{\text{n,SOC0}})|_{t=t'} \tag{34}$$

Thus, we find that Q_{CCB} at SOC0 and SOC100 shows the same upper and lower full cell OCV as well as the stoichiometry of both electrodes ($x_{\text{i,SOC100}}'$ and x_{iSOC0}') in any aged state at $t = t'$. For better understanding, a conceptual diagram of this model is depicted in Figure 1.

In conclusion, the equilibrium potential of both electrodes at a given SOC_{FC} and aged states can be expressed as

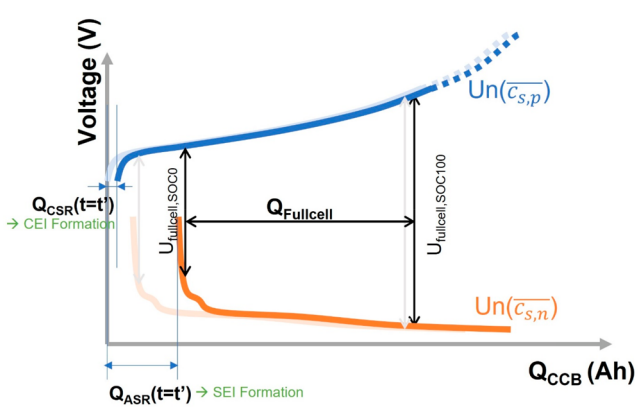

Figure 1. Conceptual diagram of the OCV model in the aged state ($t = t'$) for the positive (blue) and negative (orange) electrodes. The pale curves indicate the OCV profiles for the fresh cell ($t = 0$).

$$U_{\text{i}}(x_{\text{i,SOC}_{\text{FC}}}')|_{t=t'} = U_{\text{i}}(x'_{\text{i,SOC0}} + \text{SOC}_{\text{FC}}(x'_{\text{i,SOC100}} - x'_{\text{i,SOC0}})) \tag{35}$$

where $x_{\text{i,SOC100}}'$ and x_{iSOC0}' are dependent on $Q_{\text{ASR}}(t)$ and $Q_{\text{CSR}}(t)$.

Finally, we can derive this expression for the electrode open circuit potential for any aged state.

$$U_{\text{i}}(t) = U_{\text{i}}(\text{SOC}_{\text{FC}}, Q_{\text{ASR}}(t), Q_{\text{CSR}}(t)) \tag{36}$$

ODE System for Capacity Loss Due to Side Reactions. We can now write the side reaction equation as a coupled ordinary equation system in terms of side reaction capacity.

$$\frac{\text{d}}{\text{d}t} Q_{\text{CSR}}(t) = \frac{F}{3600} A_{\text{c}} L_{\text{p}} a_{\text{s,p}} J_{\text{CEI,0}} \times \exp\left[+\frac{\alpha_{\text{CEI}}}{RT}(U_{\text{p}}(\text{SOC}_{\text{FC}}, Q_{\text{ASR}}(t), Q_{\text{CSR}}(t)) - U_{\text{CEI}})\right] \times \exp[-\gamma_{\text{CEI}} Q_{\text{CSR}}(t)] \tag{37}$$

$$\frac{\text{d}}{\text{d}t} Q_{\text{ASR}}(t) = \frac{F}{3600} A_{\text{c}} L_{\text{n}} a_{\text{s,n}} J_{\text{SEI,0}} \times (1 + \chi_{\text{cat,Mn}} c_{\text{Mn,sol}}(t)) \times \exp\left[-\frac{\alpha_{\text{SEI}}}{RT}(U_{\text{n}}(\text{SOC}_{\text{FC}}, Q_{\text{ASR}}(t), Q_{\text{CSR}}(t)) - U_{\text{SEI}})\right] \times \exp[-\gamma_{\text{SEI}} Q_{\text{ASR}}(t)] \tag{38}$$

$$\frac{\text{d}}{\text{d}t} c_{\text{MnDsol}}(t) = \frac{a_{\text{s,p}} \epsilon_{\text{s,p}} L_{\text{p}}}{\epsilon_{\text{n}} L_{\text{n}} + \epsilon_{\text{s}} L_{\text{s}} + \epsilon_{\text{p}} L_{\text{p}}} J_{\text{MnDsol,0}} \times \exp\left[+\frac{\alpha_{\text{Mn}}}{RT}(U_{\text{p}}(\text{SOC}_{\text{FC}}, Q_{\text{ASR}}(t), Q_{\text{CSR}}(t)) - U_{\text{Mn}})\right] \tag{39}$$

with the initial conditions given by

$$Q_{\text{ASR}}(t = 0) = 0, \quad Q_{\text{CSR}}(t = 0) = 0, \quad c_{\text{MnDsol}}(t = 0) = 0 \tag{40}$$

where

$$\gamma_{\text{SEI|CEI}} = \frac{1}{2} \frac{M_{\text{SEI|CEI}}}{\rho_{\text{SEI|CEI}}} \frac{3600}{F} \frac{1}{S_{\text{i}}} \lambda_{\text{SEI|CEI}} \left[\frac{1}{\text{Ah}}\right] \tag{41}$$

Analytical Solution: Time-Invariant Approximation of Side Reactions. During calendar aging, the external current is zero, and changes in electrode stoichiometry due to side reactions and consequent losses in usable capacity occur over extremely long time scales, on the order of years. This observation allows us to further simplify the lumped model by making the reasonable assumption of a negligible change in the electrode stoichiometry. This means that the side reaction overpotentials and rate constants in eqs 37−39 can be taken as constant. The ODE system is thus written as

$$\frac{\text{d}}{\text{d}t} Q_{\text{CSR}}(t) = K_{\text{CEI}} \exp(-\gamma_{\text{CEI}} Q_{\text{CSR}}(t)) \tag{42}$$

$$\frac{\text{d}}{\text{d}t} Q_{\text{ASR}}(t) = K_{\text{SEI}}(1 + K_{\text{Mn}} t) \exp(-\gamma_{\text{SEI}} Q_{\text{ASR}}(t)) \tag{43}$$

where the approximated constants are given by

$$K_{\text{CEI}} = \frac{F}{3600} A_{\text{c}} L_{\text{p}} a_{\text{s,p}} J_{\text{CEI,0}} \exp\left[+\frac{\alpha_{\text{CEI}}}{RT}(U_{\text{p}}(\text{SOC}_{\text{FC}}, Q_{\text{side,n}}(t = 0), Q_{\text{side,p}}(t = 0)) - U_{\text{CEI}})\right] \tag{44}$$

https://doi.org/10.1021/acs.jpcc.2c07752
J. Phys. Chem. C 2023, 127, 2183−2193

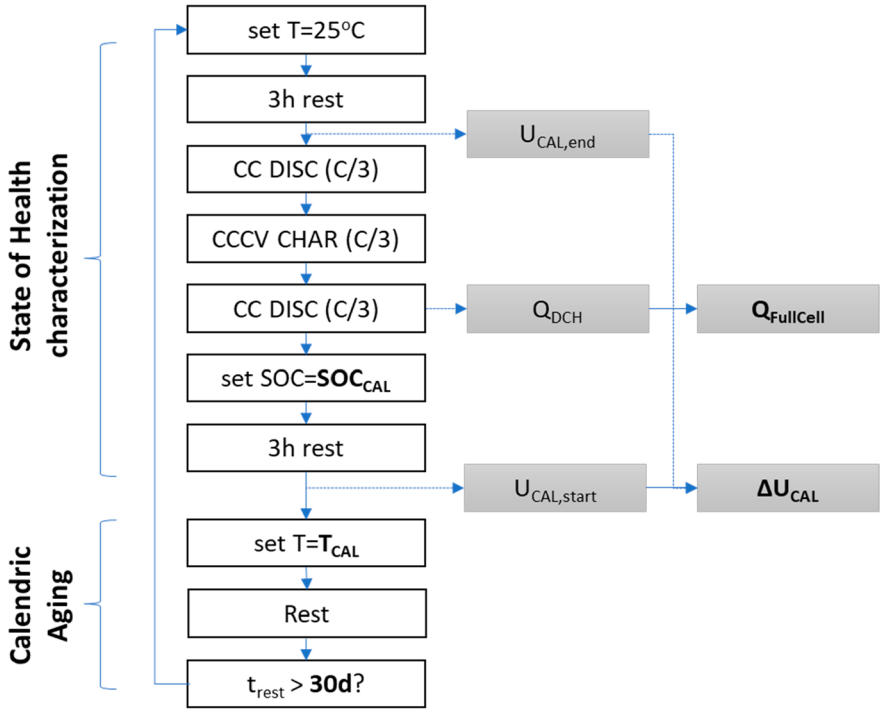

Figure 2. Schematic representation of the calendric aging test. The overall process is divided into two parts, namely, the SOH characterization and the calendric aging stage. During the characterization step, the equilibrium potential is measured, and the standard discharge capacity is measured at a C/3 rate. All characterization experiments are conducted at room temperature (25 °C). After characterization, the cell is charged to a given SOC and placed in a temperature chamber for the calendric aging step. After a fixed duration, the cell is removed from the calendric aging chamber and the SOH characterization step is repeated, thereby quantifying the capacity loss.

$$K_{SEI} = \frac{F}{3600} A_c L_n a_{s,n} J_{SEI,0} \times \exp\left[-\frac{\alpha_{SEI}}{RT}(U_n(SOC_{FC}, Q_{side,n}(t=0), Q_{side,p}(t=0)) - U_{SEI})\right] \tag{45}$$

$$K_{Mn} = \frac{a_{s,p}\epsilon_p L_p}{\epsilon_n L_n + \epsilon_s L_s + \epsilon_p L_p} J_{MnDsol,0} \times \exp\left[+\frac{\alpha_{Mn}}{RT}(U_p(SOC_{FC}, Q_{side,n}(t=0), Q_{side,p}(t=0)) - U_{Mn})\right] \tag{46}$$

We now derive a simple analytical closed form solution for the total charge lost to side reactions

$$Q_{CSR}(t) = \frac{1}{\gamma_{CEI}} \ln[1 + \gamma_{CEI} K_{CEI} t] \tag{47}$$

$$Q_{ASR}(t) = \frac{1}{\gamma_{SEI}} \ln\left[1 + \gamma_{SEI} K_{SEI} t + \gamma_{SEI} K_{SEI} K_{Mn} \frac{t^2}{2}\right] \tag{48}$$

It is worth noting that the analytical expressions in eqs 47 and 48 indicate a logarithmic dependence on time. This result aligns with the work of Broussely et al., who have also observed logarithmic capacity decay during calendar aging.[26]

Explicit Form of SOH and Self-Discharge Voltage. Full cell capacity for any aged state can be calculated not only using eq 28 but also using the approach of Sinha et al., who reported approximate equations for the relationship between side reactions and capacity decay.[14,26] The Li inventory model was derived based on the analysis of the impact of parasitic currents on the changes in discharge capacities and on the voltage drop during storage. According to this model, the relationship between remining usable capacity and side reaction capacity can be written as

$$Q_{loss}(t) = Q_{ASR}(t) - Q_{CSR}(t) \tag{49}$$

We now define the SOH as

$$SOH(t) = 1 - \frac{Q_{ASR}(t) - Q_{CSR}(t)}{Q_{full\ cell}(t=0)} \tag{50}$$

Moreover, the potential drop during the calendric aging starting at a fixed nominal SOC_{FC} can be approximated by eqs 51 and 52, from the potential differences given by the change in equilibrium potential of each electrode due to side reactions.

$$\Delta V_{self,FC} = \Delta U_{self,p} - \Delta U_{self,n} = \Delta Q_{CSR} \frac{\partial U_p}{\partial Q}\bigg|_{SOC_{FC}} - \Delta Q_{ASR} \frac{\partial U_n}{\partial Q}\bigg|_{SOC_{FC}} \tag{51}$$

$$\frac{\partial U_i}{\partial Q} = \frac{\partial U_i}{\partial x_i}\frac{\partial x_i}{\partial Q} = \frac{3600}{F c_{s,i,max} A_c L_i \epsilon_{s,i}} \frac{\partial U_i}{\partial x_i} \tag{52}$$

Here dU_j/dQ denotes the partial derivative of the capacity−OCV curve at a given solid concentration of active material or stoichiometry, and this can be derived by differentiating U_i as a function of $c_{s,i}$ or x_i. As discussed in Sinha et al., the potential drop during calendric aging is a direct measure of the electrolyte oxidation because the differential of the equilibrium potential of the anode (dU_n/dQ) is close to zero due to the plateau-like shape of the graphite OCV curve.[14] In this work, SOH was calculated using eq 50, but we observed a negligible difference even when eq 28 was used.

https://doi.org/10.1021/acs.jpcc.2c07752
J. Phys. Chem. C 2023, 127, 2183−2193

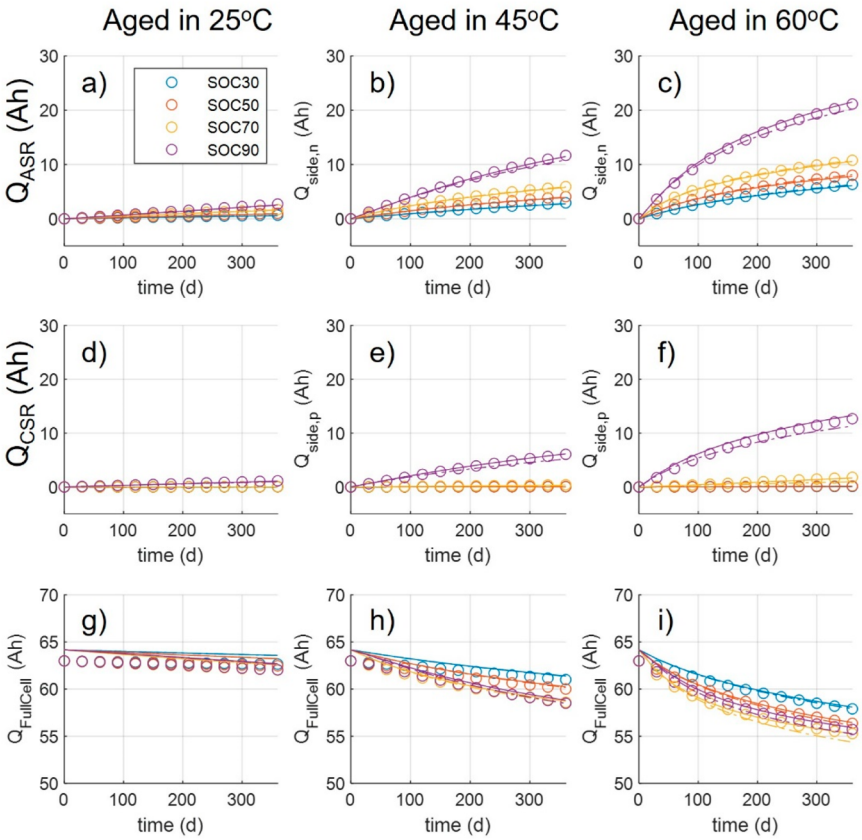

Figure 3. Comparison of calendar aging simulation results at various SOCs at 25, 45, and 60 °C. (a)−(c) Capacity loss due to the negative electrode side reactions Q_{ASR}. (d)−(f) Trends for the positive electrode side reaction. Cumulative capacity degradation trends are shown in (g)−(i). The results from the ODE (solid lines) and approximate analytical (dashed lines) forms of the lumped models are benchmarked against the single particle model (circles).

■ RESULTS AND DISCUSSION

Description of the Model Validation Process. For the validation of the lumped aging model, the SPM-based aging model was developed and used as the benchmark. The design and electrochemical parameters for the SPM battery model were selected based on a noncommercial gr/NMC cell from LG Energy Solution. The model parameters and their values are introduced in Table 1. Side reaction parameters were estimated based on calendric aging tests, and the estimated values may be found in Table 2. A discussion of the model parametrization process is beyond the scope of this work.

To simulate calendric aging with SPM, we made use of a conventional calendric aging protocol first introduced by Rumberg et al.[25] This procedure is divided into two steps, namely, the state of health characterization and calendric aging steps. In the characterization procedure, we measure the usable capacity ($Q_{\text{full cell}}$) and self-discharge potential ($\Delta V_{\text{self,FC}}$). The usable capacity is defined as the discharge capacity of the cell charged using a CC-CV protocol, with a constant current C/3 charge rate and cutoff voltage of 4.25 and where the current cutoff condition for the CV mode is C/20. The cell is then discharged at a constant C/3 rate with a voltage cutoff of 3 V to determine the discharge capacity. The self-discharge potential can be calculated from the difference between equilibrium potentials before and after calendric aging. The equilibrium potential was measured during the characterization step by obtaining the cell potential after a 3 h rest period. To set the SOC for calendric aging, we charge from the full discharged state at a constant C/3 current. The charge throughput value for the SOC setting is given by $Q_{\text{full cell}} \times \text{SOC}_{\text{CAL}}$. After the SOC condition for calendar aging is set, the calendric step begins with a 3 h rest period to allow the cell to equilibrate to the target aging temperature. The cell is then left in the target calendric aging state defined by the state of charge (SOC_{CAL}) and temperature (T_{CAL}). After t = 1 month of calendric aging, the SOH characterization step is repeated to quantify the performance decay during the calendric aging phase. A detailed schematic of this protocol is shown in Figure 2.

The SPM equations were discretized with the finite difference method, and the resulting DAEs were solved in MAPLE to simulate this calendric aging process. To simulate 1 year calendric aging, the 30 day calendric aging procedure described above was repeated 12 times. The total calendric aging period is thus t = 360 days. For the lumped aging model, we do not fully simulate the calendric aging procedure but solve only the DAEs for cathode and anode side reaction capacity (eqs 37−39). Both the usable capacity and self-discharge potential can be calculated with the implicit form of the state of health equation, eqs 51 and 52. For validation, a total of 12 calendric aging conditions (as defined by cell temperature SOC) were simulated and compared in terms of the cathode/anode side reaction loss (Q_{ASR}, Q_{CSR}) and the usable capacity of the cell ($Q_{\text{full cell}}$). The calendric aging conditions are thus combinations of three temperatures of 25, 45, and 60 °C and four SOCs of 30, 50, 70, and 90%.

https://doi.org/10.1021/acs.jpcc.2c07752
J. Phys. Chem. C 2023, 127, 2183−2193

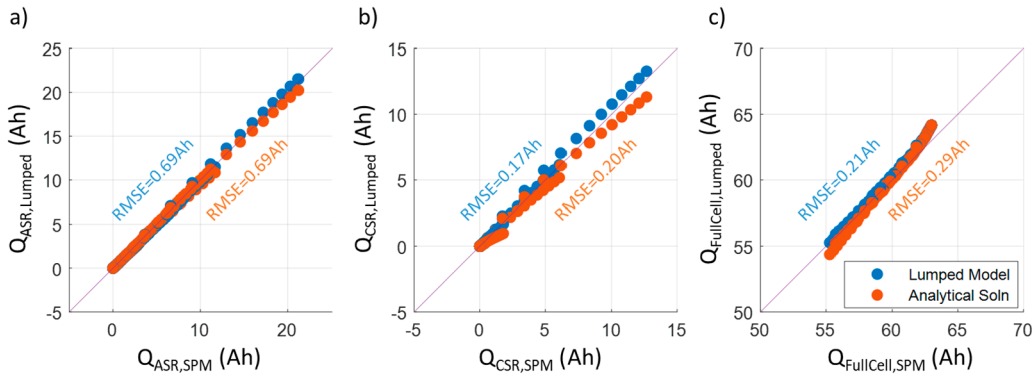

Figure 4. Error plots (parity plots) for side reaction capacities (a) Q_{ASR} and (b) Q_{CSR} and (c) cell discharge capacity $Q_{full\ cell}$. The X axis denotes the simulated value using the SPM-based degradation model, which is compared against the values from both lumped models, i.e., the lumped ODE model (blue dots), and its analytical approximation (red dots).

Model Comparisons for the State of Health for 1 Year of Calendar Aging. The lumped ODE model (eqs 37−41) and the analytical approximation (eqs 47 and 48) were simulated and compared with the SPM aging model, and these results are shown in Figure 3. Side reaction capacity losses ($Q_{ASR}(t)$ and $Q_{CSR}(t)$) exhibit a clear increase with both SOC and temperature. An increase in SOC leads to a decrease in the anode electrode potential and a corresponding decrease in the cathode electrode potential, resulting in increased side reaction rates as expected from eqs 11, 15, and 18. The Arrhenius dependence of rate constants, included in these equations, increases the side reaction rates as the temperature increases. Usable capacity trends are depicted in Figure 3g−i. Interestingly, all three models predict less capacity decay at 90% SOC relative to 70% SOC. This is because the cathode side reaction rate increases substantially for SOC > 70%, which in turn limits the total capacity loss, as also confirmed by Rumberg et al.[25]

For the 1 year calendar aging study, both side reaction losses and usable capacity trends from the lumped model show good agreement with the SPM. Side reaction capacity estimates ($Q_{ASR}(t)$ and $Q_{CSR}(t)$) show good agreement overall, but the analytical approximation shows an increase in error for higher SOCs. This can be explained by the assumption of a time-invariant equilibrium potential and reaction overpotentials, which were required in order to obtain the analytical solution. The errors associated with this assumption increase for conditions characterized by rapid aging. Furthermore, the initial usable capacity indicates a difference between the SPM and the lumped models. This is because the two models use different methods to determine usable capacity $Q_{full\ cell}$. SPM uses the discharge capacity at C/3 as the metric for usable capacity, but the lumped model uses the theoretical usable capacity defined by the OCV model. Because the C/3 discharge capacity is limited by the activation and concentration overpotential, SPM shows a lower discharge capacity. This discrepancy is expected to be substantially reduced if the same measure of usable capacity is used. This would entail updating the stoichiometry and OCV in SPM but using results from the lumped model, followed by simulating the SOH characterization step indicated in Figure 2.

An additional error analysis is summarized in Figure 4. Each graph shows model output comparisons and RMSE values. It can be seen that lumped models show acceptable errors in terms of Q_{ASR}, Q_{CSR}, and $Q_{full\ cell}$. The relative error for usable capacity ($Q_{full\ cell}$) is less than 1% of the initial capacity, and errors in prediction of side reaction capacity loss ($Q_{ASR}(t)$, $Q_{CSR}(t)$) are less than 0.5% of the usable capacity. These results thus establish the accuracy of the lumped aging model in terms of predicting calendar aging.

In terms of the simulation time, we observe significant differences between the two approaches. Simulating the SPM-based aging model for 1 year of aging typically takes approximately 50 s. In contrast, due to its reduced number of equations and explicit form of usable capacity, the lumped model in DAE form returns a degradation estimation in 0.3 s. The analytical approximation is even more efficient, completing the 1 year aging simulation in 1.2 ms. Although metrics vary depending on the hardware, platform, and numerical methods used, we can conclude that the lumped approach shows at least a 100-fold improvement in simulation time.

Incorporation of the Lumped Model into the SPM. In this section, we introduce a hybrid approach, implementing the lumped model in the SPM framework. As discussed, the lumped model shares all internal variables with a conventional electrochemical model, such as SPM. For example, we can calculate the initial value of aging-related variables, such as the thickness of the SEI/CEI layer and solid concentration of the cathode and anode after a certain calendric aging time (t_{aging}) using the proposed lumped model. As discussed earlier, given that the side reaction capacity shows good agreement, this approach is expected to yield both high accuracy and efficiency. The use of the lumped calendric aging model to initialize higher-resolution models for cycling studies is valid irrespective of the choice of the cycling model. This concept can thus also be extended to more complex electrochemical models, such as those used to simulate high-rate cycling and dynamic operating scenarios.

Mathematically, this is expressed as

$$\delta_{SEI|CEI,SPM}(t=0) = \frac{1}{2}\frac{M_{SEI|CEI}}{\rho_{SEI|CEI}}\frac{3600}{F}\frac{1}{S_n}Q_{ASR|CSR,lumped}(t=t_{aging}) \tag{53}$$

$$c_{s,i,SPM}(r,\ t=0) = c_{s,max}x_{i,lumped}(t=t_{aging}) \tag{54}$$

For the validation, two different approaches were simulated and compared. In the first case, 1 year of calendric aging was simulated using SPM, and characterization simulation was conducted for three different cases at C/3, 1C, and 2C discharge rates. In the second approach, 1 year of calendric aging was simulated using the lumped aging model, and the

https://doi.org/10.1021/acs.jpcc.2c07752
J. Phys. Chem. C 2023, 127, 2183−2193

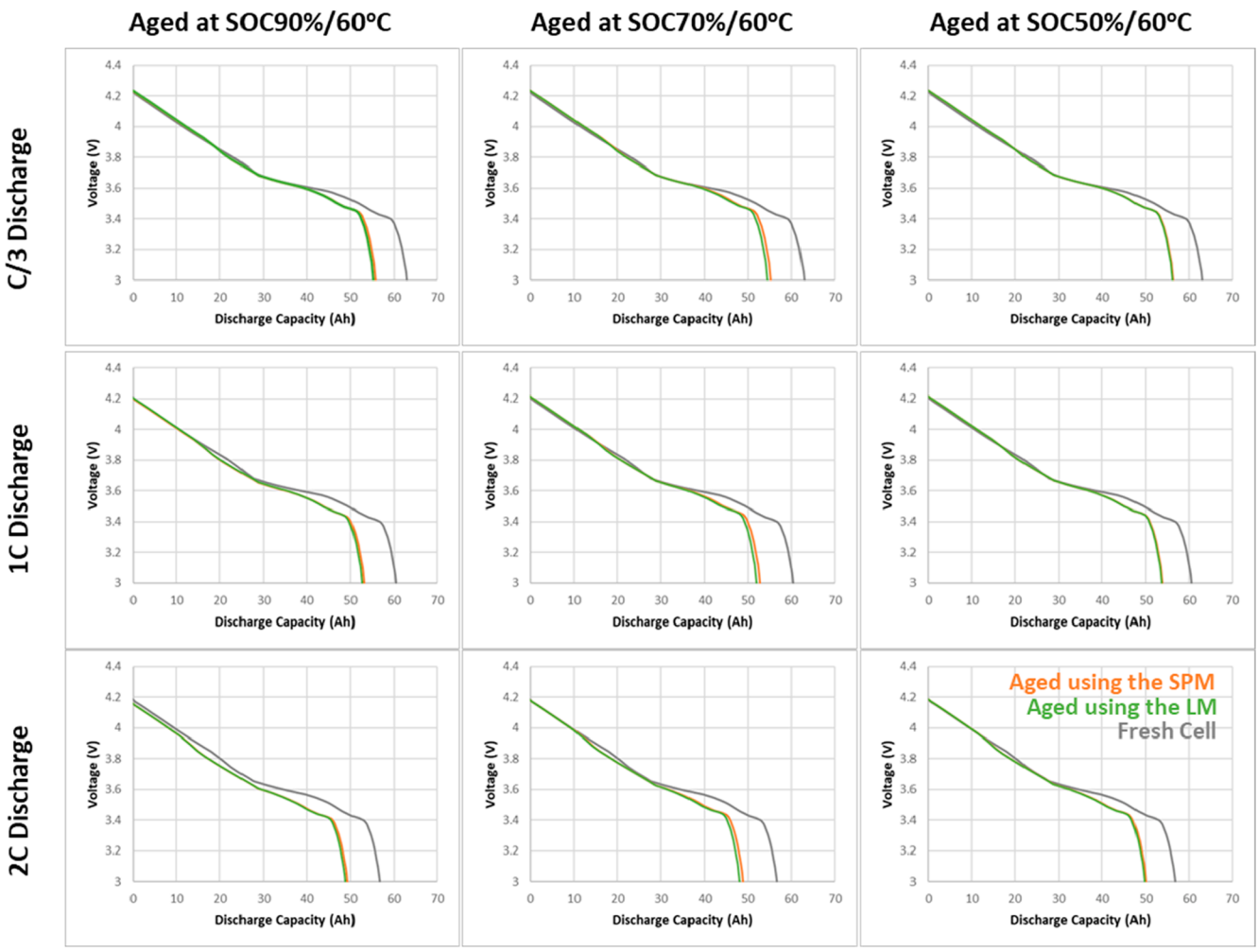

Figure 5. Discharge curves simulated using SPM for fresh (gray curves) and aged cells. The SPM was simulated for three C rates (C/3, 1C, and 2C) after simulating t = 300 days of calendar aging under the specified conditions. The green curves denote SPM initialized with results from the lumped model, while the orange curves depict simulated voltages after initialization with the SPM aging model. Note that, after initialization with the calendric aging results, the cell is first "fully charged" (based on current and voltage thresholds) before simulating the discharge curves herein.

results were then set as initial conditions for the SPM, which was again used to simulate the characterization steps at the three discharge rates. The two sets of results are compared in Figure 5. The discharge curves for the aged states expectedly indicate reduced capacity and increased polarization in comparison to the fresh cell. The discharge curves obtained with the two approaches show excellent agreement, even though the computation time with the hybrid method computation exhibits a 100-fold reduction.

■ CONCLUSIONS

An efficient electrochemical model for monitoring the state of health of Li-ion batteries under calendric aging has been introduced. The capacity fade modeling considers the SEI layer formed on the negative electrode active particle, the model that is further modified to account for the catalytic effect of dissolved manganese ions from the cathode material. The model also incorporates CEI layer growth in the positive electrode. A lumped approach for the electrochemical model has also been introduced, which uses the OCV model defined on the continuous charge balance axis coupled with the three side reactions. The lumped model results in a relatively simple ODE/DAE system which can be analytically solved by introducing a time-invariant assumption. Both the analytical and numerical lumped aging models showed a good match with the result of a benchmark SPM-based aging model in terms of the side reaction capacity and usable capacity, with 2 orders of magnitude improvement in computation time. Moreover, a hybrid method utilizing this lumped model with the higher-complexity model has been introduced. The output of an SPM simulation initialized using the variables calculated from lumped models successfully reproduced the results from the full SPM. This model can be coupled with other electrochemical models and provides a simple and efficient method to update electrochemical states to account for the effect of storage, based on well-known electrochemical calendric aging mechanisms.

■ AUTHOR INFORMATION

Corresponding Author

Venkat R. Subramanian − *Walker Department of Mechanical Engineering and Materials Science and Engineering Program, Texas Materials Institute, The University of Texas at Austin, Austin, Texas 78712, United States;* orcid.org/0000-0002-2092-9744; Phone: +1-931-349-9717; Email: venkat.subramanian@utexas.edu

https://doi.org/10.1021/acs.jpcc.2c07752
J. Phys. Chem. C 2023, 127, 2183−2193

Authors

Jin-Hyung Lim − *LG Energy Solution, Seoul 07335, Republic of South Korea*

Dongwook Koh − *LG Energy Solution, Seoul 07335, Republic of South Korea*

Suryanarayana Kolluri − *Walker Department of Mechanical Engineering and Materials Science and Engineering Program, Texas Materials Institute, The University of Texas at Austin, Austin, Texas 78712, United States*

Maitri Uppaluri − *Materials Science and Engineering Program, Texas Materials Institute, The University of Texas at Austin, Austin, Texas 78712, United States*

Akshay Subramaniam − *Walker Department of Mechanical Engineering and Materials Science and Engineering Program, Texas Materials Institute, The University of Texas at Austin, Austin, Texas 78712, United States*

Complete contact information is available at: https://pubs.acs.org/10.1021/acs.jpcc.2c07752

Notes

The results, opinions, and conclusions expressed in this work are not necessarily those of LG Energy Solution.

The authors declare no competing financial interest.

■ ACKNOWLEDGMENTS

The authors would like to acknowledge LG Energy Solution for funding support. The corresponding author (V.R.S.) received the Electrochemical Society's Battery Division's Student Research Award from Dr. Esther Takeuchi in 2001 and gratefully acknowledges her influence as an inspiration on his career.

■ GLOSSARY

Acronyms

EV	electric vehicle
NMC	nickel manganese cobalt oxide
RMSE	root-mean-square error
SEI	solid electrolyte interphase
CEI	cathode electrolyte interphase
SOC	state of charge
SOH	state of health
SPM	single particle model
ODE	ordinary differential equations
DAE	differential algebraic equations
AS	analytical solution
LM	lumped model
OCV	open circuit voltage

Symbols

A_c	cross-sectional area (m^2)
S	active surface area (m^2)
c_s	concentration of lithium in the active material particle (mol m^{-3})
c_e	concentration of solvent (mol m^{-3})
D_s	solid diffusion coefficient (m^2 s^{-1})
F	Faraday's constant (A s mol^{-1})
J_{int}	intercalation flux (mol s^{-1} m^{-2})
J_{SEI}	SEI formation flux (mol s^{-1} m^{-2})
J_{CEI}	CEI formation flux (mol s^{-1} m^{-2})
J_{MnDsol}	Mn dissolution flux (mol s^{-1} m^{-2})
I_{app}	applied current (A)
$J_{SEI,0}$	initial flux density of SEI formation (mol s^{-1} m^{-2})
$J_{CEI,0}$	initial flux density of CEI formation (mol s^{-1} m^{-2})
J_{MnDsol}	initial flux density of Mn dissolution (mol s^{-1} m^{-2})
$Q_{side,n}$	amount of charge consumed in SEI formation (Ah)
$Q_{side,p}$	amount of charge supplied by CEI formation (Ah)
Q_{loss}	loss of full cell capacity (Ah)
Q_{CCB}	continuous charge balance (Ah)
a_s	surface area per unit volume of electrode (m^{-1})
L_n	thicknesses of the negative electrode (m)
L_p	thicknesses of the positive electrode (m)
L_s	thickness of the separator (m)
M	molecular weight (kg mol^{-1})
r	coordinate along particle radius (m)
R_p	particle radius (m)
x	scaled Li concentration in solid

Greek

K_{SEI}	SEI layer conductivity (S m^{-1})
K_{CEI}	CEI layer conductivity (S m^{-1})
δ_{SEI}	SEI thickness (m)
δ_{SEI}	CEI thickness (m)
α_a	charge-transfer coefficients for oxidation
α_c	charge-transfer coefficients for reduction
χ_{CatMn}	multiplier applied to the SEI current associated with cathode Mn dissolution
ε_l	volume fraction of the electrolyte
ε_s	volume fraction of the active material in the anode or cathode
ε_f	volume fraction of the binder and filler in the anode or cathode
η	overpotential (V)
Φ	potential (V)
σ_{eff}	effective conductivity (S m^{-1})

Subscript

e	electrolyte (liquid) phase
s	solid active material
p	positive electrode
n	negative electrode
f	binder and filler
MnDsol	pertaining to the manganese dissolution reaction

■ REFERENCES

(1) Northrop, P. W. C.; Suthar, B.; Ramadesigan, V.; Santhanagopalan, S.; Braatz, R. D.; Subramanian, V. R. Efficient Simulation and Reformulation of Lithium-Ion Battery Models for Enabling Electric Transportation. *J. Electrochem. Soc.* **2014**, *161*, E3149−E3157.

(2) Kindermann, F. M.; Keil, J.; Frank, A.; Jossen, A. A SEI Modeling Approach Distinguishing between Capacity and Power Fade. *J. Electrochem. Soc.* **2017**, *164*, E287−E294.

(3) Laresgoiti, I.; Käbitz, S.; Ecker, M.; Sauer, D. U. Modeling Mechanical Degradation in Lithium Ion Batteries during Cycling: Solid Electrolyte Interphase Fracture. *J. Power Sources* **2015**, *300*, 112−122.

(4) Reniers, J. M.; Mulder, G.; Howey, D. A. Review and Performance Comparison of Mechanical-Chemical Degradation Models for Lithium-Ion Batteries. *J. Electrochem. Soc.* **2019**, *166*, A3189−A3200.

(5) Yang, X. G.; Leng, Y.; Zhang, G.; Ge, S.; Wang, C. Y. Modeling of Lithium Plating Induced Aging of Lithium-Ion Batteries: Transition from Linear to Nonlinear Aging. *J. Power Sources* **2017**, *360*, 28−40.

(6) Severson, K. A.; Attia, P. M.; Jin, N.; Perkins, N.; Jiang, B.; Yang, Z.; Chen, M. H.; Aykol, M.; Herring, P. K.; Fraggedakis, D.; Bazant, M. Z.; et al. Data-Driven Prediction of Battery Cycle Life before Capacity Degradation. *Nat. Energy* **2019**, *4*, 383−391.

(7) Santhanagopalan, S.; Guo, Q.; Ramadass, P.; White, R. E. Review of Models for Predicting the Cycling Performance of Lithium Ion Batteries. *J. Power Sources* **2006**, *156*, 620−628.

(8) Atlung, S.; West, K.; Jacobsen, T. Dynamic Aspects of Solid Solution Cathodes for Electrochemical Power Sources. *J. Electrochem. Soc.* **1979**, *126*, 1311−1320.
(9) Subramanian, V. R.; Ritter, J. A.; White, R. E. Approximate Solutions for Galvanostatic Discharge of Spherical Particles I. Constant Diffusion Coefficient. *J. Electrochem. Soc.* **2001**, *148*, E444.
(10) Northrop, P. W. C.; Ramadesigan, V.; De, S.; Subramanian, V. R. Coordinate Transformation, Orthogonal Collocation, Model Reformulation and Simulation of Electrochemical-Thermal Behavior of Lithium-Ion Battery Stacks. *J. Electrochem. Soc.* **2011**, *158*, A1461.
(11) Subramanian, V. R.; Boovaragavan, V.; Ramadesigan, V.; Arabandi, M. Mathematical Model Reformulation for Lithium-Ion Battery Simulations: Galvanostatic Boundary Conditions. *J. Electrochem. Soc.* **2009**, *156*, A260.
(12) Jung, R.; Metzger, M.; Maglia, F.; Stinner, C.; Gasteiger, H. A. Chemical versus Electrochemical Electrolyte Oxidation on NMC111, NMC622, NMC811, LNMO, and Conductive Carbon. *J. Phys. Chem. Lett.* **2017**, *8*, 4820−4825.
(13) Xu, J.; Deshpande, R. D.; Pan, J.; Cheng, Y.-T.; Battaglia, V. S. Electrode Side Reactions, Capacity Loss and Mechanical Degradation in Lithium-Ion Batteries. *J. Electrochem. Soc.* **2015**, *162*, A2026−A2035.
(14) Sinha, N. N.; Smith, A. J.; Burns, J. C.; Jain, G.; Eberman, K. W.; Scott, E.; Gardner, J. P.; Dahn, J. R. The Use of Elevated Temperature Storage Experiments to Learn about Parasitic Reactions in Wound LiCoO2/Graphite Cells. *J. Electrochem. Soc.* **2011**, *158*, A1194.
(15) Keil, P.; Jossen, A. Calendar Aging of NCA Lithium-Ion Batteries Investigated by Differential Voltage Analysis and Coulomb Tracking. *J. Electrochem. Soc.* **2017**, *164*, A6066−A6074.
(16) Rumberg, B.; Epding, B.; Stradtmann, I.; Kwade, A. Identification of Li Ion Battery Cell Aging Mechanisms by Half-Cell and Full-Cell Open-Circuit-Voltage Characteristic Analysis. *J. Energy Storage* **2019**, *25*, 100890.
(17) Lin, X.; Park, J.; Liu, L.; Lee, Y.; Sastry, A. M.; Lu, W. A Comprehensive Capacity Fade Model and Analysis for Li-Ion Batteries. *J. Electrochem. Soc.* **2013**, *160*, A1701−A1710.
(18) Safari, M.; Morcrette, M.; Teyssot, A.; Delacourt, C. Multimodal Physics-Based Aging Model for Life Prediction of Li-Ion Batteries. *J. Electrochem. Soc.* **2009**, *156*, A145.
(19) Prada, E.; Di Domenico, D.; Creff, Y.; Bernard, J.; Sauvant-Moynot, V.; Huet, F. A Simplified Electrochemical and Thermal Aging Model of LiFePO 4 -Graphite Li-Ion Batteries: Power and Capacity Fade Simulations. *J. Electrochem. Soc.* **2013**, *160*, A616−A628.
(20) Ploehn, H. J.; Ramadass, P.; White, R. E. Solvent Diffusion Model for Aging of Lithium-Ion Battery Cells. *J. Electrochem. Soc.* **2004**, *151*, A456.
(21) Ramadass, P.; Haran, B.; Gomadam, P. M.; White, R.; Popov, B. N. Development of First Principles Capacity Fade Model for Li-Ion Cells. *J. Electrochem. Soc.* **2004**, *151*, A196.
(22) Gilbert, J. A.; Shkrob, I. A.; Abraham, D. P. Transition Metal Dissolution, Ion Migration, Electrocatalytic Reduction and Capacity Loss in Lithium-Ion Full Cells. *J. Electrochem. Soc.* **2017**, *164*, A389−A399.
(23) Crawford, A. J.; Choi, D.; Balducci, P. J.; Subramanian, V. R.; Viswanathan, V. V. Lithium-Ion Battery Physics and Statistics-Based State of Health Model. *J. Power Sources* **2021**, *501*, 230032.
(24) Birkl, C. R.; McTurk, E.; Roberts, M. R.; Bruce, P. G.; Howey, D. A. A Parametric Open Circuit Voltage Model for Lithium Ion Batteries. *J. Electrochem. Soc.* **2015**, *162*, A2271−A2280.
(25) Rumberg, B.; Epding, B.; Stradtmann, I.; Schleder, M.; Kwade, A. Holistic Calendar Aging Model Parametrization Concept for Lifetime Prediction of Graphite/NMC Lithium-Ion Cells. *J. Energy Storage* **2020**, *30*, 101510.
(26) Broussely, M.; Biensan, P.; Bonhomme, F.; Blanchard, P.; Herreyre, S.; Nechev, K.; Staniewicz, R. J. Main Aging Mechanisms in Li Ion Batteries. *J. Power Sources* **2005**, *146*, 90−96.

https://doi.org/10.1021/acs.jpcc.2c07752
J. Phys. Chem. C 2023, 127, 2183−2193